DOI:10.1016/j.icarus.2019.113401

Rheological property of H_2O ice VI inferred from its self-diffusion: implications for the mantle dynamics of large icy bodies

Naoki Noguchi [1,2,†] and Takuo Okuchi [1]

[1] Institute for Planetary Materials, Okayama University,
Misasa, Tottori 682-0193, Japan

[2] Present address, Graduate School of Technology, Industrial and Social Sciences,
Tokushima University, 2-1 Minami-josanjima, Tokushima 770-8506, Japan

† Corresponding author: E-mail: noguchi.naoki@tokushima-u.ac.jp
Tel.: +81-88-656-9977 Fax: +81-0858-43-2184

ABSTRACT

The volume diffusion coefficient of water in ice VI was determined in the pressure-temperature range of 1.3 – 1.9 GPa and 300 – 320 K by in situ isotope tracer diffusion experiments. We determined the activation energy of the volume diffusion to be 61.9 ± 9.5 kJ/mol. The viscosity of polycrystalline ice VI under diffusion creep was estimated from the diffusion coefficients based on the theory of the diffusion creep. From a compilation of viscosity values in the current diffusion creep regime and the viscosity previously determined by plastic deformation experiments of ice VI in a high stress regime (Durham et al. 1996), here we provide the relationships between viscosity, stress, and the average grain size of polycrystalline ice VI. The most plausible deformation mechanism of the layers of ice VI underneath the internal oceans in large icy bodies was inferred from the viscosity-stress-average grain size relationship. We also discuss the critical thickness of the ice VI layer, which determines the onset of thermal convection.

Keywords: Ices, Mechanical properties, Interiors, Ganymede, Titan

1. INTRODUCTION

The internal oceans of large icy bodies with diameters of more than 500 km are one of the most important candidate zones for habitability in the solar system. The possibility of chemical evolution occurring in these internal oceans is promoted by the chemical and physical interactions between the oceans and the rocky mantles (Vance et al. 2007; Lammer et al. 2009). These interactions include hydrothermal alternation of the mantles, the mass exchange between the mantles and oceans, and the heat supply from the mantles. These internal oceans may resemble the submarine hydrothermal system on Earth. The plausible pressure-temperature profiles in the interiors of large icy bodies with diameters of more than 2000 km suggest the existence of layers of high-pressure ice underneath the internal oceans (Noack et al. 2016; Vance et al. 2018). These high-pressure ice layers may inhibit the above-described ocean-rock interactions. Many numerical studies of interior planetary structures based on observations made by spacecraft have inferred the existence of such high-pressure ice layers (e.g., Tobie et al. 2006; Lefèvre 2014; Choblet et al. 2017; Kalousovä et al. 2018). In particular, among the pressure-temperature phases of H_2O, ice VI has a relatively wide stability region that can form thick layers over 100 km deep in the large icy bodies. Thus, understanding the viscosity of polycrystalline ice VI is essential because it controls thermal history and dynamics of these thick ice VI layers, thus affecting habitability in the interiors of the large icy bodies. Furthermore, understanding the viscosity of polycrystalline ice VI is required for undertaking the Jupiter Icy Moons Explorer mission (JUICE) scheduled for the 2030s. During the mission, a tidal deformation measurement has been planned to prove the existence of an internal ocean in Ganymede (Grasset et al. 2012). Assuming an interior structure without an internal ocean, the tidal response will depend on the viscosity of ice VI (Kamata et al. 2016).

52 The viscosity of polycrystalline ice VI under low-stress conditions is the most important
53 parameter for understanding the dynamics of the ice VI layer, because the stress induced by the
54 buoyancy-driven thermal convection in large icy bodies was estimated to be below 0.1 MPa (Sotin
55 and Tobie 2004; McCarthy and Castillo-Rogez 2013; Choblet et al. 2017; Kalousovä et al. 2018).
56 However, deformation experiments under such low-stress conditions are technically very difficult.
57 Durham et al. (1996) investigated the rheological properties of high-pressure ices V and VI using a
58 high-pressure gas medium deformation apparatus. They revealed viscosities and plastic deformation
59 mechanisms of polycrystalline ices V and VI in the range of 0.1 – 100 MPa. The viscosity of each
60 phase under high stress conditions is controlled by dislocation creep or the reduction of grain size
61 by recrystallization (Durham et al. 1996). The deformation rate of ice VI under this high-stress
62 creep regime is stress-dependent with the stress exponent of 4.5, and is insensitive to the average
63 grain size (Durham et al. 1996). The extrapolation of the plastic-flow law under this mechanism
64 into the lower stress conditions may give an overestimate for the viscosity, because the diffusion
65 creep can dominate under lower stress conditions of 0.1 MPa (Sotin and Tobie 2004; McCarthy and
66 Castillo-Rogez 2013). Under the diffusion creep regime, the viscosity of ice VI behaves as a
67 Newtonian fluid, which is sensitive to the grain size. Although the viscosity under the diffusion
68 creep regime cannot be measured directly, it can be quantitatively determined from the volume
69 diffusion coefficient of the molecules constituting the deforming material, as proposed by the
70 theories of diffusion creep (Frost and Ashby 1982). We therefore measured the diffusion coefficient
71 of ice VI in an isotope tracer diffusion experiment to determine its viscosity under the high-pressure
72 conditions of the large icy body interiors.
73 Conventional isotope diffusion methodology using mass spectrometers (e.g., Farver and

74 Yund 1991) cannot be applied for high-pressure conditions because it requires a high vacuum
75 environment. To address this problem, we used micro-Raman spectroscopy to develop an isotope
76 tracer diffusion method that has the potential to be an isotope probe for the high-pressure samples in
77 a diamond anvil cell (DAC). This method has been applied to diffusion studies for various hydrous
78 minerals (Noguchi and Shinoda 2010; Guo et al. 2013; Pilorgé et al. 2017; Ganzhorn et al. 2018).
79 First, to conduct the diffusion experiments for the high-pressure ices, an analytical method to
80 quantify isotope tracers using micro-Raman spectroscopy was developed (Noguchi and Shinoda
81 2010; Noguchi et al. 2016). We have successfully applied this method to tracer diffusion
82 experiments of ice VII using DAC, yielding the proton diffusion coefficient up to 17 GPa (Noguchi
83 and Okuchi 2016). In this study, we applied the technique to conduct hydrogen tracer diffusion
84 experiments for ice VI. We report the diffusion coefficients of water molecules of ice VI and its
85 viscosity under the diffusion creep regime. In addition, we discuss the condition required to trigger
86 convection in large icy bodies based on the temperature-dependence of viscosity.
87
88 **2. EXPERIMENTAL METHODS**
89 **2.1. Diffusion experiment**
90 A Mao-Bell type DAC was used to generate the pressure. The DAC was equipped with a
91 pair of type-IIa diamond anvils with a 600 μm diameter culet. A pre-indented Re foil with a sample
92 chamber of approximately 200 μm in diameter was used as a gasket. The thicknesses of the sample
93 chambers were in the range of 70 – 90 μm. Diffusion couples in each sample chamber were
94 prepared under low-humidity within a freezer cooled down to 252 K. A commercial isotope-tracer
95 reagent (D_2O; 99.9 %, Wako Co. Ltd.) was used. The detailed methodology for preparing diffusion

couples was reported by Noguchi and Okuchi (2016). The schematic drawing of the diffusion couple in the sample chamber is shown in **Fig. 1**. Firstly, D_2O ice was made in the sample chamber. Several grains of ruby were also added to the chamber as the pressure marker (Mao et al. 1978). A hole of approximately 100 μm in diameter was drilled in the isotope-tracer ice by using a hot micro-pin. A micro ball of H_2O ice approximately 200 μm in diameter was prepared by freeze spraying. The micro ball was dropped into the hole of the isotope-tracer ice. Finally, the diffusion couple was pressurized to approximately 5 GPa at the temperature below the triple point for liquid, ice I_h, and ice III. The diffusion couples of ice VII were transformed to ice VI by decreasing the pressure. The grains in the polycrystalline ice VI were grown at approximately 1 GPa and at 293 K which are the conditions near the melting point. Several grains with an average size range of 50 – 100 μm were released in the sample chamber (**Fig. 1**). In some cases, we succeeded in making a diffusion couple composed of a single crystal, where grains of H_2O and D_2O ices were fused. The DAC was then kept at 300 or 320 K in a constant temperature bath or a vacuum-oven to promote self-diffusion. Pressure was repeatedly measured after keeping the sample for up to 10 h, and was adjusted to maintain the pre-defined pressure through one diffusion experiment. Experimental conditions are listed in **Table 1**.

2.2. Raman spectroscopy

A micro Raman spectroscope is composed of an optical microscope (Eclipse LV150, Nikon Co. Ltd.) equipped with a motor-driven X-Y sample stage (SGSP20-35, Sigma Koki Co. Ltd.), a 532 nm DPSS laser (100 mW, J100GS-1H-17-23, Showa Optronics Co. Ltd.), a notch filter, and a polychromator (Spectra-Pro-300i, Acton Research Co. Ltd.) with a focal length of 30 cm. The

polychromator was equipped with a charge-coupled device (CCD) with an image resolution of 100 × 1340 pixels (RS, Roper Co. Ltd). Diffractive grating of 1200 grooves/mm was selected for the Raman measurement. The laser beam was focused through an objective lens with a ×50 magnification (TPlan SLWD 50×, N.A. = 0.40, Nikon Co. Ltd.). The laser power at the focal point was approximately 10 mW for the Raman measurements. At this laser power, we confirmed that optical heating never melted the ice. The effective lateral and vertical resolutions of the measurement in the DAC were 2.1 and 10.5 μm, respectively (Noguchi and Okuchi 2016). On the tracer diffusion experiment, the spatial resolution of the probe is an important factor for estimating the real tracer-diffusion coefficient (Ganguly et al. 1988).

The two-dimensional Raman mapping measurements of the diffusion couples in the DAC were carried out using point-by-point illumination through sequential translation of the sample stage. The position and shape of H_2O/D_2O boundary could not be accurately established in the ice diffusion couples. Visualizing the distribution of the concentration of the isotope tracers by the mapping measurement was essential to be able to estimate the diffusion coefficient (**Fig. 1**). The laser beam was focused on the middle plane of the sample chamber to exclude any interference brought about by diffusion through the interface between the anvil surface and the diffusion couple.

The standard area dimension of Raman mapping was 80 × 100 μm^2, composed of grids of 2 × 2 μm^2. The exposure time for each measurement point was 3–5 s, and the total time needed to complete one Raman map was approximately 6 h. The diffusion of water in ice VI during the Raman mapping was negligible, because the diffusion length at room temperature for 6 h estimated from the diffusion coefficient and discussed in a later section, is less than 1 μm.

2.3. Quantitative analysis of deuterium concentration

A calibration curve was constructed to determine the molar concentration of deuterium (c_{OD} = D/(H+D)) from the micro-Raman spectrum. Several Raman spectra of ice VI of known c_{OD} values were measured at 1.4 GPa to construct the calibration curve (**Fig. 2a**). Raman bands related to OD and OH stretching modes appeared in the ranges of 2120–2710 cm^{-1} and 2800–3600 cm^{-1}, respectively. The OD stretching band overlapped with the multiphonon second-order Raman band of diamond (**Fig. SA1a** in Noguchi and Okuchi 2016). The relative area ratio of the OD stretching band to OH stretching band is expressed as:

$$A_{ratio} = \frac{A_{OD}}{A_{OD}+A_{OH}} \quad , \quad (1)$$

where A_{OD} and A_{OH} are the areas under the Raman bands for OD and OH stretching modes, respectively. The ratio was used as the index for determining c_{OD}. A correction due to the overlapping of the Raman band of diamond on the estimate for A_{OD} was performed using the height of the edge of the diamond Raman band at the high-wavenumber side, as reported by Noguchi and Okuchi (2016). The c_{OD} was then plotted as a function of A_{ratio} in **Fig. 2b**. Although the shapes of the Raman bands depend on the crystallographic orientation of the ice grain, we confirmed that the relative area ratio (A_{ratio}) is independent of the orientation. Thus, the crystallographic orientation did not affect the calibration line. However, another problem for the quantitative analysis is the presence of a "dead zone" in the range of $0.65 < c_{OD} < 0.8$, where c_{OD} is not very sensitive to A_{ratio} (**Fig. 2b**). Hence, a deuterium-rich water with a composition of $(H_{0.4},D_{0.6})_2O$ was prepared and used in all of the diffusion experiments. In so doing, we avoided the problem of using that part of the calibration line within the dead zone. Expressed as a quartic function, the calibrated relationship between the c_{OD} and the A_{ratio} when $c_{OD} < 0.65$ becomes:

$$c_{OD} = 4.4192{A_{ratio}}^4 - 5.0012{A_{ratio}}^3 + 1.8429{A_{ratio}}^2 + 0.8603A_{ratio} \quad . \quad (2)$$

The shapes and intensities of the Raman bands of the OH and OD stretching modes depend on c_{OD} because of intermolecular coupling interactions (**Fig. 2a**), which are the cause of the nonlinearity of the calibration curve. The molecular coupling interaction is induced where the same molecular type adjoins in the crystal lattice, namely, H_2O…H_2O or D_2O…D_2O, and the frequencies of the OH or OD stretching modes of these molecules are modulated slightly (Horning et al. 1958; Bertie and Whally 1964; Noguchi and Okuchi 2016). Since the probability that molecules of the same type adjoin in $(H,D)_2O$ ice depends on c_{OD}, the shapes of the Raman bands vary with c_{OD}.

3. RESULTS

The representative optical photographs of the diffusion couples are shown in **Fig. 3**. During the diffusion experiments, the grain boundaries can reorder or migrate through recrystallization processes that depend on the thermodynamic stability of grain shapes. However, such changes of the polycrystalline textures were not observed during the diffusion experiments.

The two-dimensional c_{OD} distributions were determined from the area ratio of the OD stretching mode to the OH stretching mode using the calibration curve (**Figs. 3a-c**). It is noteworthy that signs of leakage of the tracer from grain boundaries to grain interiors appeared in the two-dimensional c_{OD} distributions (**Figs. 3a** and **b**). Such leakage is an indication of fast grain-boundary diffusivity. Although we currently acknowledge the difficulty of determining the grain-boundary diffusion coefficient for the complex geometry of the grain boundaries, it may be determined by numerical analysis in the future. The volume diffusion coefficient of hydrogen (D_V)

was determined from the two-dimensional c_{OD} distributions. We first selected a rectangular area 6 μm wide and 80 μm in typical length, which was cut from each two-dimensional diffusion map to include the H_2O/D_2O boundary perpendicular to the longer axis of the rectangle (dotted yellow rectangles in **Figs. 3a-c**). We then integrated the c_{OD} values within each rectangle in the direction parallel to the H_2O/D_2O boundary (**Figs. 4a-c**). The ideal one-dimensional diffusion profile is expressed as the solution to the following diffusion equation:

$$c_{OD}(x,t) = \frac{1}{l}\int_0^l f\left(x'\right)dx' \quad + \frac{2}{l}\sum_{n=1}^{\infty} \exp\left(-\frac{D_V n^2\pi^2 t}{l^2}\right)\cos\frac{n\pi x}{l}\int_0^l f\left(x'\right)\cos\frac{n\pi x'}{l}dx' \ , \quad (3)$$

where $f(x)$ is the initial distribution, l is the length of a diffusion couple, and t is time (Crank 1956). The initial distribution was converted to $f(x)$ by fitting a Fourier series. The diameters of the sample chambers were used as the value of l. The measured diffusion profiles were affected by the spatial resolution. According to Ganguly et al. (1988), the resultant diffusion profile can be expressed as the convolution of the ideal diffusion profile and Gaussian function as follows:

$$g(x) = \frac{1}{\sqrt{2\pi}\sigma}\exp\left(-\frac{x^2}{2\sigma^2}\right) \ , \quad (4)$$

$$c_{conv}(x,t) = \int_{-\infty}^{\infty} c_{OD}\left(x',t\right)\cdot g(x'-x)dx' \ , \quad (5)$$

where σ is a factor that accounts for the effective lateral resolution of the instrument. The value of σ was determined to be 2.1 μm from the result of the edge scan test using quartz (Noguchi and Okuchi 2016). The value of D_V for each run was determined by least-squares fitting of the one-dimensional diffusion profile with **Eq. 5** (**Table 1**).

The activation energy and frequency factor (pre-exponential factor) were determined from the slope and intercept of the Arrhenius plot of D_V (**Fig. 5**). Our measured Arrhenius equation

is:

$$D_V = 2.1 \times 10^{-6} \exp\left[-\frac{61.9 \pm 9.5 \text{ kJ/mol}}{RT}\right] \text{ (m}^2\text{/s)}, \quad (6)$$

where R is the gas constant. The activation energy is relatively large compared to that of ice I_h (58 kJ/mol; Itagaki 1967; Ramseier 1967). In the pressure range of 1.3 – 1.9 GPa, pressure dependence of D_V was not observed (**Table 1**).

4. DISCUSSION

4.1. Viscosity of polycrystalline ice VI

The convective vigor of the ice VI layers in large icy bodies depends on the deformation mechanism of polycrystalline ice VI and the temperature dependence of its viscosity. To elucidate the dominant deformation mechanism of plastic flow in the polycrystalline ice VI layer, we estimated the viscosity as a function of deviatoric stress (σ) and average grain size (d). In a high stress regime, viscosity can be derived from the plastic-flow law determined previously in a deformation experiment (Durham et al. 1996); while in a low stress regime, the viscosity should be derived from the plastic-flow law of the diffusion creep. The relationship between strain rate and stress in the diffusion creep regime can be express as follows (Nabarro-Herring creep: Herring, 1950):

$$\dot{\varepsilon} = A\,\sigma/d^2, \quad (7a)$$

$$A = 14\Omega D_V/RT, \quad (7b)$$

where $\dot{\varepsilon}$, D_V, and Ω are the strain rate, the volume diffusion coefficient of the rate-controlling atom or molecule, and the volume of one vacancy that can be approximated by the molar volume (Fortes et al. 2012), respectively. The strain rate is controlled by the D_V of the slowest diffusion species in a

material. Estimating viscosity using **Eqs. 7a** and **b** requires understanding of the diffusion mechanism of ice VI at the atomic level.

In the case of ice I_h, the free interstitial molecule mechanism is accepted as the dominant diffusion mechanism (e.g., Onsarger and Runnels 1963; Ikeda-Fukazawa et al. 2002). Moreover, the similarity between the D_V values of ^3H and ^{18}O of ice I_h (Delibaltas et al., 1966) indicates that the volume diffusion of the whole H_2O molecule is the deformation-controlling process. In the case of ice VII, the dominant diffusion mechanism changes with increasing pressure. Below 10 GPa and at 300 K, the migration of the whole H_2O molecule is the dominant mechanism (Hernandez and Caracas 2018); above 10 GPa, protonic diffusion becomes the dominant mechanism (Katoh et al. 2002; Noguchi and Okuchi 2016). Between the two, the protonic diffusion process is more complex, with the formation of ionic defects, H_3O^+ and OH^-; and the migration of rotational defects, D and L. The oxygen atom in the H_2O molecule is the deformation-controlling species in the protonic diffusion mechanism. In this case, the diffusion mechanism is affected by the hydrogen bond distance and density (Hernandez and Caracas 2018). The hydrogen bond distance and density of ice VI (Kuhs et al. 1984; Fortes et al. 2012) are intermediate between those of ice I_h at ambient pressure and ice VII at 10 GPa. Thus, in the case of ice VI, the migration of the whole H_2O molecule must be the dominant mechanism. We therefore consider the hydrogen diffusion coefficient determined by this study (D_V) as the volume diffusion coefficient of the H_2O molecule.

The viscosity ($\eta = 2\sigma/\dot{\varepsilon}$) of ice VI was calculated using **Eqs. 7a** and **b**. Grain-size sensitive creep, which has been reported for ices I_h and II (Durham et al. 2001; Goldsby and Kohlstedt 2001; Kubo et al. 2006), was not considered when the viscosity was estimated because it was not reported in a previous deformation experiment on ice VI (Durham et al. 1996). The $\eta - \sigma -$

249 d relationships at 1.2 GPa, 270 K and at 1.2 GPa, 300 K are shown in **Fig. 6**. Their
250 pressure-temperature conditions are relevant in the middle part of the ice VI layer with thicknesses
251 of 200 and 500 km, which occur within Titan and Ganymede, respectively (Tobie at al. 2006;
252 Choblet et al. 2017; Kalousovä et al. 2018).

253 As inferred from the **Fig. 6** constraining the two parameters controlling viscosity, σ and d,
254 is key to elucidating the deformation mechanism in the ice VI layer. Plausible convective stresses in
255 the ice VI layers were previously estimated from the buoyancy, which range from 1 kPa to 0.1 MPa
256 (Sotin and Tobie 2004; McCarthy and Castillo-Rogez 2013; Choblet et al. 2017; Kalousovä et al.
257 2018). On the other hand, the grain size is a kinetic parameter that must vary with time after the
258 initial planetary differentiation process. However, in the case of terrestrial ice I_h, the grain boundary
259 pinning by particles of impurities controls the final grain size (Barr and Mckinnon 2007a; Kubo et
260 al. 2009). Polycrystalline ices in sheets includes insoluble impurities of ~5×10^{-4} wt%, and their
261 grain sizes are typically within the range of 1 – 10 mm (e.g., Durand et al. 2006; Duval 2013).
262 Similar to this case, here we assume a huge quantity of particles of salt hydrates and silicates must
263 blend into the ice VI layer during the differentiation of the ice bodies. If this assumption is correct,
264 then the grain size of ice VI may be comparable to that of the terrestrial ice. Thus, the assumption
265 that the grain size does not exceed a few meters is very possible. Consequently, the most plausible
266 deformation mechanism inferred from the results in **Fig. 6** is diffusion creep.

267

268 **4.2. Convective criterion in the ice VI layer**

269 Here, we discuss the criterion for the onset of thermal convection in the ice VI layer
270 according to Newtonian rheology. The critical Rayleigh number for a Newtonian fluid is

$Ra_{cr} = 20.9\theta^4$, (8a)

$\theta = E\Delta T/RT_b^2$, (8b)

where T_b is the basal temperature of the ice VI layer, ΔT is the temperature difference across the layer, E is the activation energy for the plastic deformation, which is equal to the activation energy of the volume diffusion coefficient (Solomatov 1995). Using this critical Rayleigh number and the relationship between strain rate and stress, the critical layer thickness, $D_{cr,}$ above which thermal convection can occur, is estimated as follows:

$$D_{cr} = \left(\frac{Ra_{cr} k d^2 \exp(\frac{E}{RT_b})}{3A\rho g \alpha \Delta T} \right)^{1/3}, \quad (9)$$

where A is the pre-exponential constant of the plastic-flow low (**Eq. 7b**), k is the thermal diffusivity, ρ is the density, g is the local gravity acceleration, and α is the thermal expansivity (Barr and Pappalardo 2005; Solomatov and Barr 2006; Barr and Mckinnon 2007b). All parameters in **Eq. 9** except for the g and ΔT have been determined in previous and current experiments. The values for g and ΔT are constrained, based on the evolution models of Titan by Tobie et al. (2006) and Ganymede by Kalousovä et al. (2018). The radii of the silicates mantles of Titan and Ganymede have been estimated to be about 1800 km. Furthermore, the valid value for g at the interface between the silicate mantles and the ice VI layers is 1.6 m/s^2 (Kalousovä et al. 2018). Based on the thermal histories of Titan and Ganymede after differentiation (**Fig. 7**), the predicted ΔT is in the range of 15 to 30 K, while T_b falls within the range of 260 to 300 K. These parameters used for the calculation are shown in **Table 2**. D_{cr} as a function of d is shown in **Fig. 7**. During the evolution of large icy bodies, the onset of the convection of the ice VI layer occurred when its thickness exceeded a few km, as long as the final d was kept within the order of 10 mm as mentioned above

(**Fig. 7**). Thus, the heat from the silicate mantle was efficiently transported to the internal ocean. Previous geophysical studies suggest that the current Titan and Ganymede have ice VI layers of at least over 100 km thick (Tobie et al. 2006; Lefèvre 2014; Choblet et al. 2017; Kalousovä et al. 2018). Therefore, thermal convection must currently be actively occurring in their ice VI layers.

5. CONCLUSIONS

We determined the volume diffusion coefficient of ice VI using a DAC and micro-Raman spectroscopy. This method has been applied in diffusion studies of other high-pressure ice phases such as ices II, III, V. Furthermore, the viscosity of polycrystalline ice VI was inferred from the diffusion parameters determined here and the deformation parameters determined by a previous deformation experiment (Durham et al. 1996). Assuming realistic values of convective stress and d in the ice VI layer of large icy bodies, we conclude that diffusion creep is the mechanism currently controlling plastic-flow. We also determined the critical thickness of the ice VI layer for convection based on Newtonian rheology. Considering the uncertainty associated with estimates of d values discussed within the context of deformation mechanisms, there is a need to conduct experiments on the grain growth of polycrystalline ice VI in order to more reliably address the dynamics of large icy bodies.

ACKNOWLEDGEMENTS

N. N. would like to thank Dr. S. Kamata of Hokkaido University for fruitful discussions. This work was financially supported by the Grant-in-Aids (nos. 15K17795, 17K14422, 17H06456) from the Japan Society for Promotion of Science.

REFERENCES

Barr, A.C., Pappalardo, R.T., 2005. Onset of convection in the icy Galilean satellites: influence of rheology. J. Geophys. Res. 110, E12005, doi:10.1029/2004JE002371.

Barr, A.C., McKinnon, W.B., 2007a. Convection in ice I shells and mantles with self-consistent grain size. J. Geophys. Res. 112, E02012, doi:10.1029/2006JE002781.

Barr, A.C., McKinnon, W.B., 2007b. Convection in Enceladus' ice shell: Conditions for initiation. Geophys. Res. Lett. 34, L09202, doi:10.1029/2006GL028799.

Bertie, J.E., Whally, E., 1964. Infrared spectra of ices I_h and I_c in the range 4000 to 350 cm^{-1}. J. Chem. Phys. 40, 1637–1645.

Choblet, G., Tobie, G., Sotin, C., Kalousová, K., Grasset, O., 2017. Heat transport in the high-pressure ice mantle of large icy moons. Icarus 285, 252–262.

Choukroun, M., Grasset, O., 2010. Thermodynamic data and modeling of the water and ammonia-water phase diagrams up to 2.2 GPa for planetary geophysics. J. Chem. Phys. 133, 144502–1–13.

Crank, K., 1956. Mathematics of diffusion. Oxford University Press, New York.

Delibaltas, P., Dengel, O., Helmreich D., Riehl, N., Simmon, H., 1966. Diffusion von ^{18}O in Eis-Einkristallen. Phys. Condens. Mater. 5, 166–170.

Durand, G., Weiss, J., Lipenkov, V., Barnola, J.M., Krinner, G., Parrenin, F., Delmonte, B., Ritz, C., Duval, P., Röthlisberger, R., Bigler, M., 2006. Effect of impurities on grain growth in cold ice sheets. J. Geophys. Res. 111 (F1), 1–18.

Durham, W.B., Stern, L.A., Kirby, S.H., 1996. Rheology of water ices V and VI. J. Geophys. Res. 101, 2989–3001.

Durham, W.B., Stern, L.A., Kirby, S.H., 2001. Rheology of ice I at low stress and elevated confining pressure. J. Geophys. Res. 106 (6), 11031–11042.

Duval, P., 2013. Creep behavior of ice in polar ice sheets. In: Gudipati, M.S., Castillo-Rogez, J. (Eds.), The Science of Solar System Ices. Springer, pp. 227–251.

Farver, J.R., Yund, R.A., 1991. Measurement of oxygen grain boundary diffusion in natural, fine-grained, quartz aggregates. Geochim. Cosmochim. Acta 55, 1597–1607.

Fortes, A.D., Wood, I.G., Tucker, M.G., Marshall, W.G., 2012. The P–V–T equation of state of D_2O ice VI determined by neutron powder diffraction in the range $0 < P < 2.6$ GPa and $120 < T < 330$ K, and the isothermal equation of state of D_2O ice VII from 2 to 7 GPa at room temperature, J. Appl. Cryst. 45, 523–534.

Frost, H.J., Ashby, M.F., 1982. Deformation Mechanism Maps. Pergamon, Tarrytown, New York.

Ganguly, J., Bhattacharya, R.N., Chakraborty, S., 1988. Convolution effect in the determination of compositional profiles and diffusion coefficients by microprobe step scans. Am. Mineral. 73, 901–909.

Ganzhorn, A.C., Pilorge, H., Floch, S.L., Montagnac, G., Cardon, H., Reynard, B., 2018. Deuterium-hydrogen inter-diffusion in chlorite, Chem. Geol. 493, 518–524.

Goldsby, D., Kohlstedt, D., 2001. Superplastic deformation of ice: Experimental observations. J. Geophys. Res. 106, 11017–11030.

Grasset, O., Dougherty, M., Coustenis, A., Bunce, E., Erd, C., Titov, D., Blanc, M., Coates, A., Drossart, P., Fletcher, L., et al., 2013. Jupiter icy moons explorer (JUICE): An ESA mission to orbit Ganymede and to characterize the Jupiter system. Plan. Space Sci. 78, 1–21.

Guo, X., Yoshino, T., Okuchi, T., Tomioka, N., 2013. H-D interdiffusion in brucite at pressures up to 15 GPa. Am. Mineral. 98, 1919–1929.

Hernandez, J.A., Caracas, R., 2018. Proton dynamics and the phase diagram of dense water ice. J. Chem. Phys. 148, 214501–1–11.

Herring, C., 1950. Diffusional viscosity of a polycrystalline solid. J. Appl. Phys. 21, 437–445.

Hornig, D.F., White, H.F., Reding, F.P., 1958. The infrared spectra of crystalline H_2O, D_2O and HDO. Spectrochim. Acta 12, 338–349.

Ikeda-Fukazawa, T., Horikawa, S., Hondoh, T., Kawamura, K., 2002. Molecular dynamics studies of molecular diffusion in Ice I_h. J. Chem. Phys. 117, 3886–3896.

Itagaki, K., 1967. Self-diffusion in single crystal ice. J. Phys. Soc. Jpn. 22, 427–431.

Kalousovä, K., Sotin, C., Choblet, G., Tobie, G., Grasset, O., 2018. Two-phase convection in Ganymede's high-pressure ice layer – Implications for its geological evolution. Icarus 299, 133–147.

Kamata, S., Kimura, J., Matsumoto, K., Nimmo, F., Kuramoto, K., Namiki, N., 2016. Tidal deformation of Ganymede: Sensitivity of Love numbers on the interior structure. J. Geophys. Res. 121, 1362–1375.

401 Katoh, E., Yamawaki, H., Fujihisa, H., Sakashita, M., Aoki, K., 2002. Protonic diffusion in
402 high-pressure ice VII. Science 295, 1264–1266.
403
404 Kubo, T., Durham, W.B., Stern, L.A., Kirby, S.H., 2006. Grain Size–Sensitive Creep in Ice II.
405 Science 311, 1267–1269.
406
407 Kubo, T., Nakata, H., Kato, T., 2009. Effects of insoluble particles on grain growth in
408 polycrystalline ice: Implications for rheology of ice shells of icy satellites. J. Mineral. Petrol. Sci.
409 104, 301–306.
410
411 Kuhs, W.F., Finney, J.L., Vettier, C., Bliss, D.V., 1984. Structure and hydrogen ordering in ices VI,
412 VII and VIII by neutron powder diffraction, J. Chem. Phys. 81, 3612–3623.
413
414 Lammer, H., Bredehöft, J., Coustenis, A., Khodachenko, M., Kaltenegger, L., Grasset, O., Prieur, D.,
415 Raulin, F., Ehrenfreund, P., Yamauchi, M., Wahlund, J.E., Grießmeier, J.M., Stangl, G., Cockell,
416 C.S., Kulikov, Y.N., Grenfell, J.L., Rauer, H., 2009. What makes a planet habitable? Astron.
417 Astrophys. Rev. 17, 181–249.
418
419 Lefèvre, A., Tobie, G., Choblet, G., ˇCadek, O., 2014. Structure and dynamics of Titan's outer icy
420 shell constrained from Cassini data. Icarus 237, 16–28.
421
422 McCarthy, C., Castillo-Rogez, J., 2013. Planetary ices attenuation properties. In: Gudipati, M.S.,
423 Castillo-Rogez, J. (Eds.), The Science of Solar System Ices. Springer, pp. 183–225.
424
425 Mao, H.K., Bell, P.M., Shaner, J.W., Steinberg, D.J., 1978. Specific volume measurements of Cu,
426 Mo, Pd, and Ag and calibration of the ruby R_1 fluorescence pressure gauge from 0.06 to 1 Mbar, J.
427 Appl. Phys. 49, 3276–3283.
428
429 Noack, L., Höning, D., Rivoldini A., Heistarcher, C., Zimov, N., Journaux, B., Lammer, H., Hoolst,

T.V., Bredehöft, J.H., 2016. Water-rich: How habitable is a water layer deeper than on Earth? Icarus 277, 215–236.

Noguchi, N., Kubo, T., Durham, W.B., Kagi, H., Shimizu, I., 2016. Self-diffusion of polycrystalline ice I_h under confining pressure: hydrogen isotope analysis using 2-D Raman imaging. Phys. Earth. Planet. Inter. 257, 40–47.

Noguchi, N., Okuchi, T., 2016. Self-diffusion of protons in H_2O ice VII at high pressures: Anomaly around 10 GPa. J. Chem. Phys. 144, 234503–1–9.

Noguchi, N., Shinoda, K., 2010. Proton migration in portlandite inferred from activation energy of self-diffusion and potential energy curve of OH bond. Phys. Chem. Mineral. 37, 361–370.

Onsarger, L., Runnels, L.K., 1963. Mechanism for self-diffusion in ice. Proc. Natl. Acad. Sci. U.S. 50, 208–210.

Pilorgé, H., Reynard B., Remusat L., Lefloch, S., Montagnac G., Cardon H., 2017. D/H diffusion in serpentine. Geochim. Cosmochim. Acta 211, 355–372.

Ramseier, R.O., 1967. Self-diffusion of tritium in natural and synthetic ice monocrystals. J. Appl. Phys. 38, 2553–2556.

Ross, R.G., Andersson, P., Bäckström, G., 1978. Effects of H and D order on the ther- mal conductivity of ice phases. J. Chem. Phys. 68, 3967–3972.

Solomatov, V. S., 1995. Scaling of temperature- and stress-dependent viscosity, Phys. Fluids, 7, 266–274.

Solomatov, V. S., Barr, A.C., 2006. Onset of convection in fluids with strongly

459 temperature-dependent, power-law viscosity. Phys. Earth Planet. Int. 155, 140–145.
460
461 Sotin, C., Tobie, G., 2004. Internal structure and dynamics of the large icy satellites. Comptes
462 Rendus Phys. 5 (7), 769–780.
463
464 Tobie, G., Lunine, J., Sotin, C., 2006. Episodic outgassing as the source of atmospheric methane on
465 Titan. Nature 440, 62–64. doi: 10.1038/nature04497 .
466
467 Vance, S., Harnmeijer, J., Kimura, J., Hussmann, H., DeMartin, B., Brown, J.M., 2007.
468 Hydrothermal systems in small ocean planets. Astrobiology 7, 987–1005.
469
470 Vance, S., Panning, M.P., Stähler, S., Cammarano, F., Bills, B.G., Tobie, G., Kamata, S., Kedar, S.,
471 Sotin, C., Pike, W.T., Lorenz, R., Huang, H.H., Jackson, J.M., Banerdt, B., 2018. Geophysical
472 investigations of habitability in ice‐covered ocean worlds. J. Geophys. Res. Planet. 123, 180–205.
473

474 **TABLE**

475

TABLE I. Experimental conditions and hydrogen diffusion coefficients of ice VI (D_V).

Run No.	Isotope	T (K)	P (GPa)	Total t (h)	D_V (m^2/s)
1	D_2O[a]	300	1.30 ± 0.15	162.0	$(4.3 \pm 0.0) \times 10^{-17}$
2	D_2O	300	1.55 ± 0.12	553.0	$(3.5 \pm 0.3) \times 10^{-17}$
3	D_2O	300	1.88 ± 0.02	575.2	$(2.1 \pm 0.5) \times 10^{-17}$
4	D_2O	300	1.90 ± 0.03	1171.2	$(5.5 \pm 1.1) \times 10^{-17}$
5	D_2O	320	1.75 ± 0.12	250.0	$(1.9 \pm 0.9) \times 10^{-16}$
6	D_2O	320	1.87 ± 0.02	222.3	$(2.3 \pm 0.8) \times 10^{-16}$
7	D_2O	320	1.88 ± 0.02	202.2	$(1.4 \pm 0.1) \times 10^{-16}$
8	D_2O	320	1.89 ± 0.03	343.3	$(1.4 \pm 0.5) \times 10^{-16}$

[a] True composition was $(H_{0.4},D_{0.6})_2O$ (see text).

476

TABLE 2. List of parameters used in the calculation of the critical thickness (D_{cr}).

Symbol	Physical property	Value	Unit
T_b	Basal temperature of the ice VI layer[a]	260 – 290	K
ΔT	Temperature difference across the layer[a]	15 – 30	K
P	Pressure[a]	1.2	GPa
g	Gravity acceleration[a]	1.6	m/s^2
E	Activation energy of diffusion[b]	61.9	kJ/mol
α	Thermal expansivity[c]	$1.9–2.1 \times 10^{-4}$	1/K
k	Thermal diffusivity[d]	$4.6–5.2 \times 10^{-7}$	m/s^2
ρ	Density[c]	1370–1380	kg/m^3

[a] See text.

[b] This study.

[c] Fortes et al. (2012)

[d] Ros et al. (1978)

477

478

FIGURE CAPTIONS

FIGURE 1. Schematic drawing of the diffusion couple prepared within the sample chamber of the diamond anvil cell (DAC).

FIGURE 2. Raman spectra of $(H,D)_2O$ measured at 1.4 GPa and at room temperature (**a**). c_{OD} indicates the molar deuterium concentration (D/(H+D)). (**b**) Correlation between A_{ratio} and c_{OD} for $(H,D)_2O$ ices. A_{ratio} indicates the relative area ratio of the OD stretching band to OH stretching band. The dotted line shows the calibration line, which was determined by fitting a quartic function to the averaged data with respect to pressure (**Eq. 2**).

FIGURE 3. Polarized-light optical photographs of the diffusion couples of polycrystalline ice VI (the far-left column) and two-dimensional maps of c_{OD} (molar ratio of D_2O) of the diffusion couples: **a**) Run. 4 (**Table 1**), **b**) Run. 6, **c**) Run. 7. Rectangles in the photographs show the coverage of the Raman mapping measurements. Scale bars represent 50 μm. The black regions in **a** and **b,** where the word "Ruby" is printed, are the regions where the intense fluorescence light from the ruby interfered with Raman measurements.

FIGURE 4. One-dimensional hydrogen diffusion profiles (**a** – **c**) calculated from the data enclosed by the yellow-dotted rectangular area in **Figs. 3a** – **c**, respectively. The solid lines, except for the lines for 0 h, indicate the least squares fit of **Eq. 5** to the data. The lines for 0 h are $f(x)$, which was determined by fitting a Fourier series to the initial distribution.

FIGURE 5. Arrhenius plot of D_V of ice VI (**Table 1**).

FIGURE 6. Viscosities of polycrystalline ice VI at 1.2 GPa, 270 K and at 1.2 GPa, 300 K. The homologous temperatures at 270 K and 300 K correspond to 0.87 and 0.96, respectively (Choukroun and Grasset 2010). The lines of the dislocation creep were calculated using the

parameters taken from Durham et al. (1996). The gray and reddish bands of the dislocation creep represent the error arising from the activation energy error of the dislocation creep.

FIGURE 7. Critical thickness of the ice VI layer in the large icy bodies for convection (D_{cr}).

Fig.1

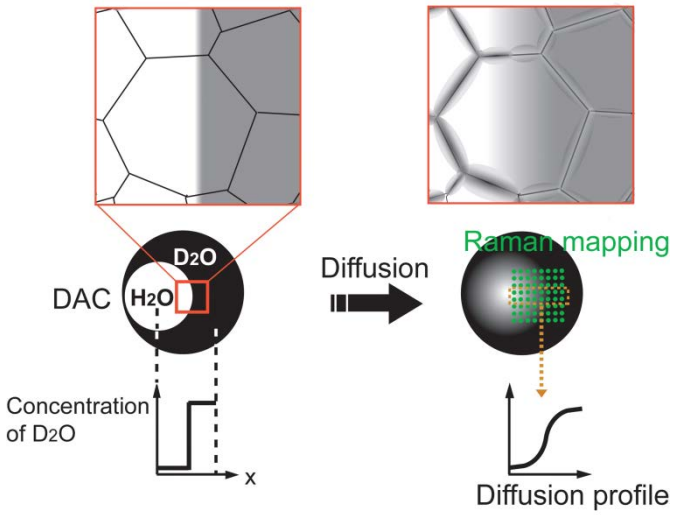

Fig. 2

Fig.3

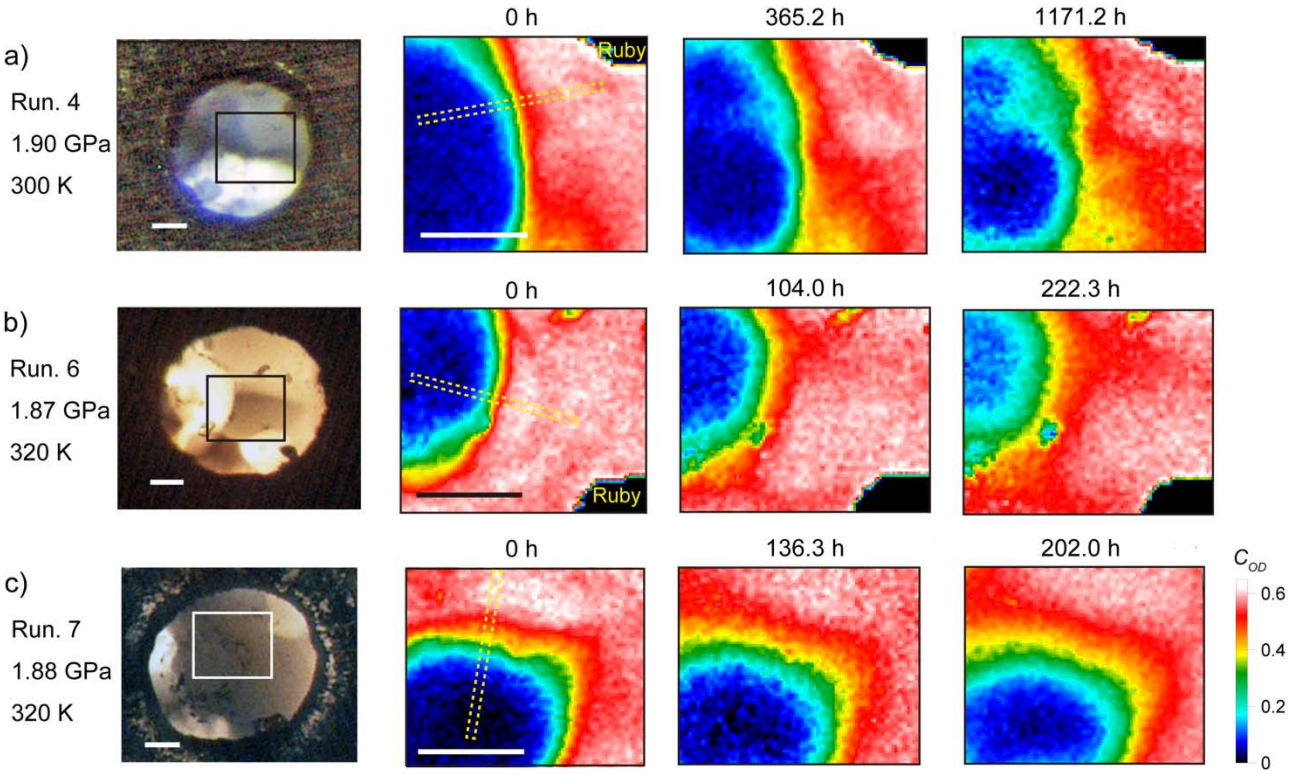
a)
Run. 4
1.90 GPa
300 K
0 h
365.2 h
1171.2 h
Ruby
b)
Run. 6
1.87 GPa
320 K
0 h
104.0 h
222.3 h
Ruby
c)
Run. 7
1.88 GPa
320 K
0 h
136.3 h
202.0 h
C_{OD}
0.6
0.4
0.2
0

Fig.4

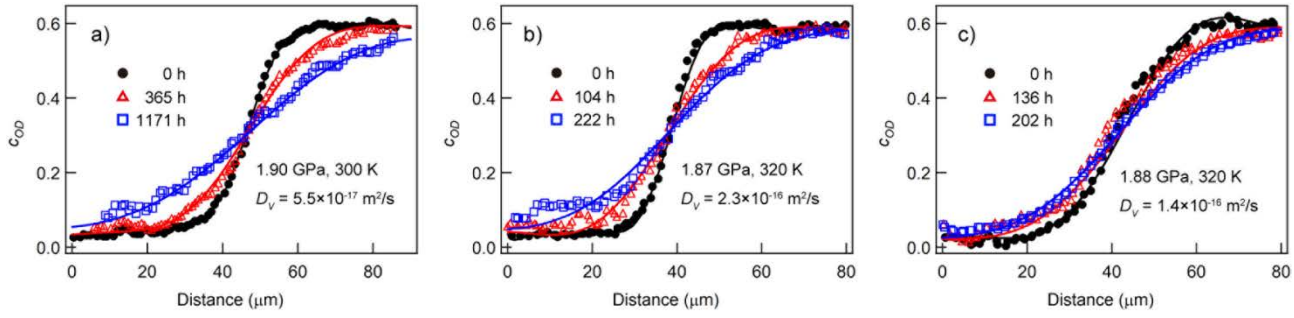
a)
0 h
365 h
1171 h
1.90 GPa, 300 K
D_V = 5.5×10^{-17} m^2/s
b)
0 h
104 h
222 h
1.87 GPa, 320 K
D_V = 2.3×10^{-16} m^2/s
c)
0 h
136 h
202 h
1.88 GPa, 320 K
D_V = 1.4×10^{-16} m^2/s
C_{OD}
Distance (μm)

Fig. 5

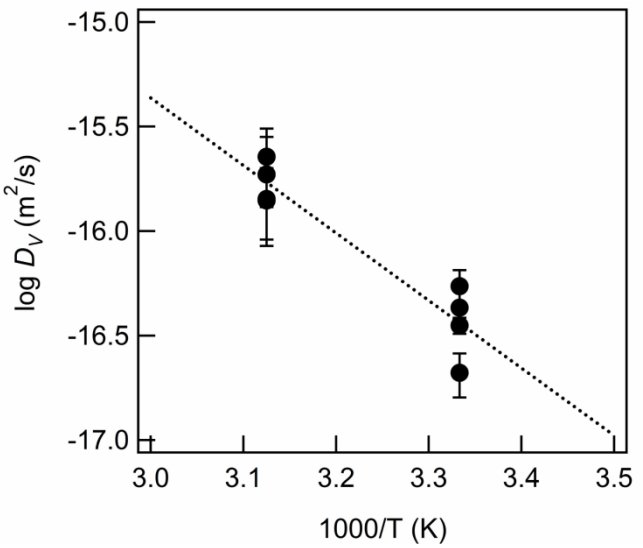
-15.0
-15.5
-16.0
-16.5
-17.0
log D_V (m^2/s)
3.0
3.1
3.2
3.3
3.4
3.5
1000/T (K)

Fig. 6

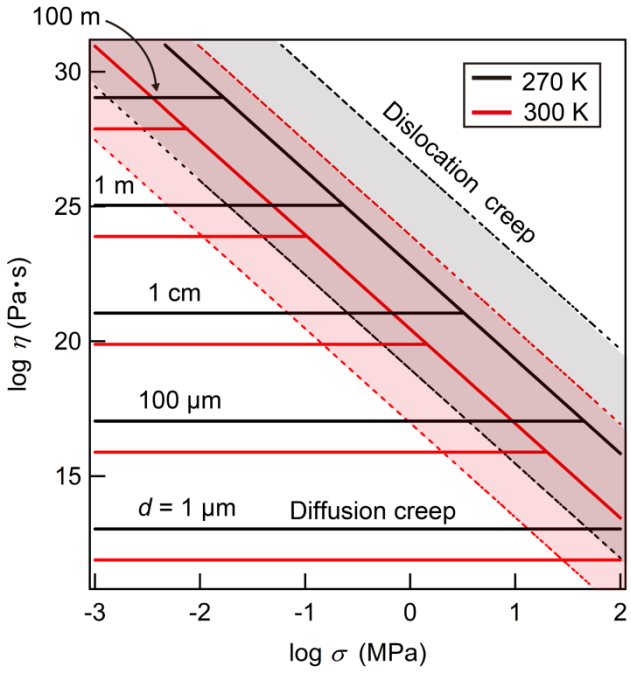
100 m
30
25
20
15
1 m
1 cm
100 μm
d = 1 μm
Diffusion creep
Dislocation creep
270 K
300 K
log η (Pa·s)
-3
-2
-1
0
1
2
log σ (MPa)

534 **Fig. 7**

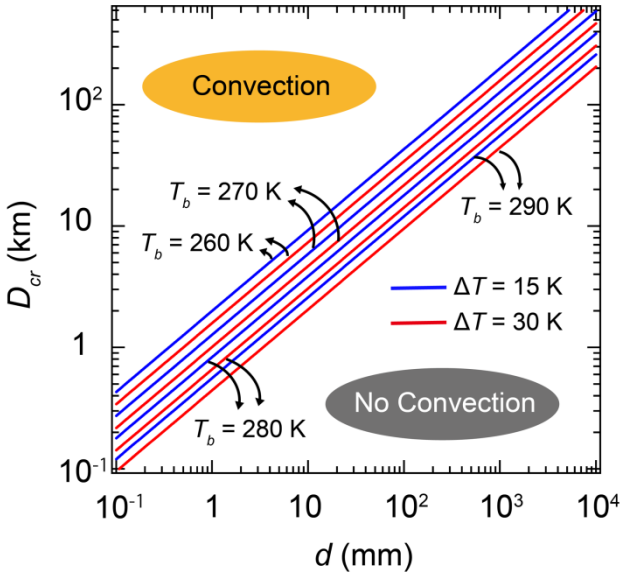
Convection
No Convection
T_b = 270 K
T_b = 260 K
T_b = 290 K
T_b = 280 K
ΔT = 15 K
ΔT = 30 K
D_{cr} (km)
d (mm)
10^{-1}
1
10
10^2
10^3
10^4

535